

# Sub-THz Power Amplifiers: Measurements, Behavioral Modeling and Predistortion Algorithms

Lutfi Samara<sup>1,2</sup>, Simon Haussmann<sup>3</sup>, Erind Tufa<sup>4</sup>, Antonio Alberto D'Amico<sup>4,5</sup>, Tommaso Zugno<sup>1</sup>, Ingmar Kallfass<sup>3</sup>, Thomas Kürner<sup>2</sup>

<sup>1</sup>Munich Research Center, Huawei Technologies, Munich, Germany

<sup>2</sup>Technische Universität Braunschweig, Braunschweig, Germany

<sup>3</sup>University of Stuttgart, Inst. of Robust Power Semiconductor Systems, Stuttgart, Germany

<sup>4</sup>Dipartimento di Ingegneria dell'Informazione, University of Pisa, Pisa, Italy

<sup>5</sup>National Inter-University Consortium for Telecommunications (CNIT), Parma, Italy

Emails: {lutfi.samara,tommaso.zugno}@huawei.com,{simon.haussmann,ingmar.kallfass}@ilh.uni-stuttgart.de,erind.tufa@phd.unipi.it, antonio.damico@unipi.it, t.kuerner@tu-braunschweig.de

**Abstract**—With global IMT traffic expected to grow 10-100 times from 2020 to 2030<sup>1</sup>, the Terahertz (THz) spectrum offers a promising solution to satisfy such forecasts. However, occupying the THz spectrum comes with its own challenges, an important one being impairments caused by broadband RF components in THz transceivers. Nonlinearities in power amplifiers (PAs) complicate meeting link budget requirements, with amplitude and phase distortions degrading the system's performance, especially when adopting waveforms with high peak-to-average power ratios (PAPRs), such as Orthogonal Frequency Division Multiplexing (OFDM). In this paper, we present characterization results of a 300 GHz PA using small-signal and large-signal continuous-wave measurements. Models capturing Amplitude-to-Amplitude Modulation (AM-AM) and Amplitude-to-Phase Modulation (AM-PM) behavior across 270-330 GHz are developed and verified with wideband measurements, confirming the compression behavior, while nonetheless showing inaccuracies for low input powers due to unaccounted frequency dependencies. Based on the derived models, a predistortion algorithm is designed and analyzed, revealing significant error performance degradation when switching between single- and multi-carrier waveforms. We finally show that an appropriate selection of predistorter parameters can significantly improve the performance.

**Index Terms**—modeling, power amplifiers, pre-distortion, terahertz.

## I. INTRODUCTION

Terahertz (THz) frequency bands are currently considered as a means to satisfy the always increasing demand for higher data rates and overcome the spectrum scarcity problem faced by traditional wireless systems [2]. The International Telecommunication Union (ITU) already identified a total of 137 GHz between 275 and 450 GHz for mobile and fixed services, and further concessions are expected in the near future [3]. The wide bandwidth available at these frequencies can be exploited to deliver extremely high communication performance, achieving data rates up to terabits-per seconds and ultra-low latency. Thanks to the enhanced directionality, THz systems can reduce interference and achieve higher spatial reuse. In addition, the small size of antennas at these

frequencies enables the fabrication of compact transceivers suitable for small-scale applications. Further, the short wavelength and unique propagation properties of THz signals make them ideal for precise sensing and localization, positioning this technology as a promising candidate for implementing integrated sensing and communication functionalities.

The sub-THz technology has already been considered for establishing point-to-point and short range wireless connections. The IEEE developed a standard operating between 252 and 325 GHz and supporting channel bandwidths up to 69 GHz [4]. The target applications include wireless front/backhauling, wireless data centers, kiosk downloading, and intra-device communications. Other potential use cases have been identified by different research and industrial initiatives, including cooperative mobile robots, eXtended Reality (XR), wireless data centers, real-time industrial control at the edge, and virtual commissioning of industrial plants with hardware in the loop [5], [6], [2].

The exploitation of this frequency range comes with a set of challenges, including harsh and variable propagation conditions experienced over wireless channels and pronounced hardware impairments faced by sub-THz components. In [7], several impairments have been analyzed, including oscillator phase noise, antenna beamsquinting, and power amplifier nonlinearities. If not properly treated, such defects can limit the achievable performance and hinder the full exploitation of the sub-THz frequency bands. In this regard, the Power Amplifier (PA) is one of the most critical components in the Radio Frequency (RF) chain. Ideally, the PA should increase the power of the modulated signal. However, PAs operating at sub-THz frequencies exhibit pronounced non-linearity effects, leading to unwanted signal distortion when operating at high power levels. On the other hand it is advantageous to operate the PA near the compression region due to increased power efficiency. This is particularly relevant when adopting multi-carrier waveforms such as OFDM, in which large amplitude fluctuations in the modulated signal – high Peak-to-Average Power Ratio (PAPR) – may strain the PA and cause significant distortion. Moreover, when operating over wide bandwidths, PAs may exhibit memory effects which further distort the input signal.

This work has been performed in part in the framework of the HORIZON-JU-SNS-2022 project TIMES, co-funded by the European Union. Views and opinions expressed are however those of the author(s) only and do not necessarily reflect those of the European Union.

<sup>1</sup>Forecasts are reported in [1].

These effects can be compensated by adopting linearization techniques such as signal predistortion, which applies an inverse transformation to the input signal in the baseband domain before entering the power amplification stage. The first step for implementing this technique is to evaluate the non-linear behavior of the PA and develop suitable amplitude and phase distortion models. A common approach is to conduct measurement for characterizing the PA device and use the empirical data to extract suitable behavioral models describing the input-output relationships.

#### A. Pre-existing models and prior art

For the evaluation of the NR waveform performance, the 3GPP adopted the polynomial model described in [8]. Although it has been derived from empirical measurements at sub-6 GHz, this model has been recommended by 3GPP also for carrier frequencies above 6 GHz. Since it has been derived from measurements with input power between -35 and 9 dBm, it may not provide accurate results outside this range. An alternative Rapp model for above-6 GHz evaluations was proposed in [9], however, it was considered less appropriate than the sub-6 GHz polynomial model since, although being more accurate than a simple clipping model, the applicability of the Rapp approach was questioned in the case of wideband operations.

Metrology and device characterization in the sub-THz band is restricted mostly to Continuous Wave (CW) measurements or two-tone measurements. At high millimeter-wave frequencies, measurements are performed mostly indirectly with frequency extension modules or other frequency conversion units, while analyzing the data at much lower frequency. In [10], [11], authors measured the input-output relationship of a SiGe PA operating at 290 GHz. The results were used to derive the parameters of popular memoryless/quasi-memoryless models, including Rapp, Ghorbani, White, and Saleh models. The authors claim that the Rapp model provides the best trade-off between accuracy and model validity, as it shows a meaningful behavior for input power levels outside of the measurement range.

Recently, the European Telecommunications Standards Institute (ETSI) has established an industry specification group on the topic of THz, named ETSI ISG THz, where in a recently published report on RF impairments [7], it extended the modified Rapp model proposed in [9] by collecting the performance metrics of several sub-THz PAs operating between 100 and 200 GHz that are available in the literature. The collected data was used to derive the parameters of the average AM-AM distortion characteristic.

The non-linear PA behavior is considered as a key issue for enabling efficient and reliable THz/sub-THz communications [12], [13]. Previous works compared the performance of different Physical (PHY) layer waveforms under PA non-idealities. The Rapp model proposed by 3GPP was used in [14] and [15] for the evaluation of different single and multi-carrier waveforms. In [16], authors used a simple cubic PA model to compare the performance of OFDM and single carrier waveforms in a multi-antenna system. The authors of [17]

presented an analysis of different modulation schemes for THz communications where the saturation effect of the PA is considered by applying a PAPR penalty to the input signal. Results show that low-order modulation schemes perform best but pay in terms of spectral efficiency.

#### B. Contributions of this work

Characterizing PAs operating at sub-THz frequencies presents significant challenges due to difficulties in the measurement process. Measurement benches capable of properly isolating the PA behavior and providing accurate results at such high frequencies are difficult to set up. The lack of measurement data prevents the extrapolation of suitable behavioral models and their validation. Most of the models available in the literature are derived from measurements taken at lower frequencies which are unable to properly capture the PA behavior at sub-THz.

In this paper, a characterization of a PA operating at 300 GHz is performed based on small-signal and large-signal continuous-wave measurements. The tested device is a 300-GHz Indium Gallium Arsenide (InGaAs) metamorphic high-electron mobility transistor (mHEMT) PA [18], [19]. Several models are derived that yield AM-AM and AM-PM behavior for several frequency bands spanning the 270 to 330 GHz frequency range. Measurements obtained by adopting a Vector Network Analyzer (VNA)-based cross-domain measurement platform (Reported in [20], [21], [22] and [23]) demonstrate novel characterization capabilities under broadband-modulated conditions and compare the simulation results based on the derived models with the measurements. Based on the derived models, a predistortion algorithm is derived and tested considering single and multi-carrier waveforms while varying various performance metrics.

The contributions presented in this paper are summarized as follows:

- We make use of a novel cross-domain characterization method, which is able to reduce the influence of the measurement setup and the thermal noise contribution to a negligible level, making an isolated view on the Device Under Test (DUT) possible while using wideband modulated data. In Section III, we present detailed measurement data showing significant changes in the behavior of a THz-PA over the frequency of operation. This data is publicly available [24] to facilitate possible standardization processes.
- In Section IV, we propose multiple system-level models and evaluate them comprehensively on the basis of the measured data. We provide the model parameters and make them publicly available in [24], and verify the derived models using results from wideband measurements. We further perform a comparison with different available models in the literature and discuss this comparison.
- In Section V, a predistortion algorithm is designed based on the derived models. Implications on the application of predistortion on the performance of single- and multi-carrier waveforms are shown, thus addressing an open question on the applicability of multi-carrier waveforms at such frequencies.

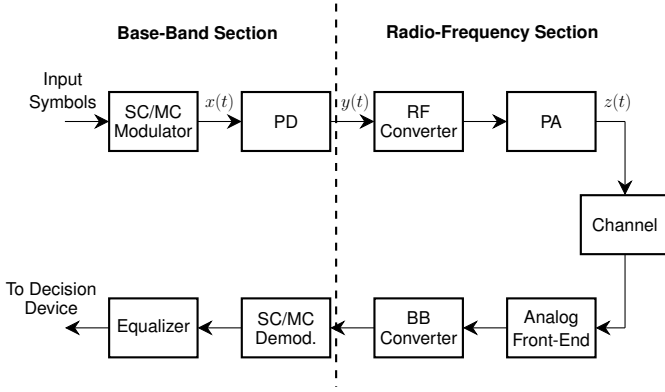


Fig. 1: Schematic diagram of the communication system under investigation.

Initial results of this work were presented in [23], where the same measurement setup was used to characterize the 300-GHz InGaAs mHEMT power amplifier at a single operating frequency (280 GHz), and only the parameters for the polynomial and the modified Rapp models were derived. On the other hand, in this study we report new results for several frequencies within the 60 GHz bandwidth from 270 to 330 GHz, and we use these measurements to derive the parameters of the polynomial and modified Rapp models, along with the Saleh and Ghorbani models, which were not taken into consideration in [23]. Also, the analysis of communication systems employing pre-distortion algorithms to compensate the PA non-linearities was not present in [23].

## II. COMMUNICATION SYSTEM MODEL

Fig. 1 shows a schematic diagram of the communication system under investigation. The input symbols, which typically belong to an  $M$ -QAM constellation, are fed to a modulator that produces the continuous-time waveform,  $x(t)$ . Here we consider both single-carrier and multi-carrier modulations. The latter are efficiently implemented through an OFDM architecture which uses fast Fourier transform (FFT) algorithms. A detailed description of standard single-carrier and OFDM transmitters, with bi-dimensional constellations, can be found in many textbooks, e.g., [25]. Essential components of the communication system in Fig. 1 are the predistortion device and the PA, which operates at sub-THz frequencies.

The predistortion algorithm works on the baseband equivalent of the RF signal while amplification is performed on the up-converted signal, before transmission over the channel.

The electromagnetic waveform at the output of the propagation medium is converted to an electric signal by the receive antenna, and then processed through a standard receiver, as shown in the lower part of Fig. 1. In particular, after baseband (BB) conversion and demodulation, the signal samples are equalized before they are sent to the decision device.

In considering the communication system reported in Fig. 1, the main objective is that of comparing the performance of single-carrier and multi-carrier waveforms at sub-THz frequencies, in the presence of a predistortion algorithm. It is well-known that, with respect to a single-carrier system, the

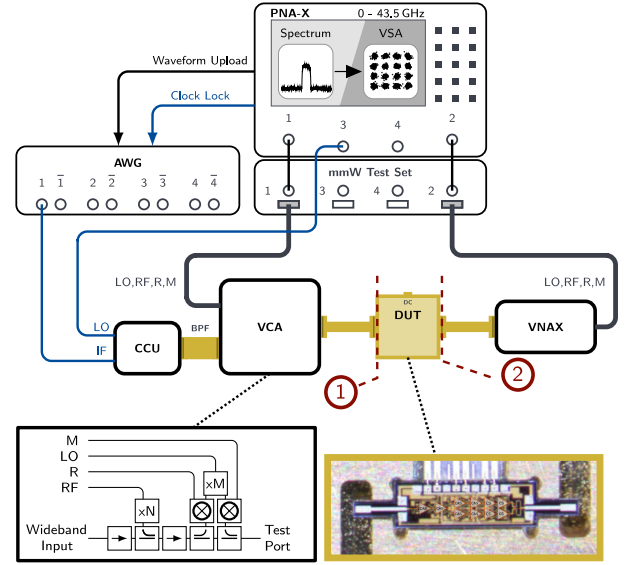


Fig. 2: Block diagram of the cross-domain setup for CW as well as wideband-modulated characterization of the H-band amplifier DUT, with calibration planes 1 at the input and 2 at the output (from [23]).

OFDM signal is characterized by a much higher PAPR, and this results in severe distortions in passing through the PA. In a frequency-flat channel single-carrier systems are undoubtedly the better choice. On the other hand, multi-carrier modulations could be preferable in the presence of a frequency-selective behavior of the propagation medium, due, for example, to frequency-dependent molecular absorption, or simply to an environment with rich scattering, as demonstrated in [26]. Accordingly, in the context of sub-THz communications, it becomes very important to accurately analyze the performance of single-carrier and multi-carrier waveforms that consider effective techniques for the compensation of PA non-linearities.

## III. CHARACTERIZATION OF A THz-POWER AMPLIFIER

The scope of this section is focused on the evaluation of the influence of the non-linearities of the THz-PA for the extraction of system-level models. For device characterization in the sub-THz domain, frequency-extension modules are usually used to increase the frequency range of the base unit. Using vector calibration methods, the influence of the up- and down-conversion of the signal as well as other impairments in the signal generation or acquisition can be minimized and an isolated view on the DUT is possible. This procedure can be applied to CW characterization of sub-THz devices. However, an important aspect of our work is also the measured validation of the extracted system-models, while being excited with wideband modulated data. This is enabled by a cross-domain measurement testbench, which is described in more detail in [20], [21], [22] and [23]. Fig. 2 shows the block diagram of the characterization setup. The input and the output of the DUT are connected via WR-3.4 waveguide interfaces to the VNAX (VNA Extension Module) and VCA (Vector Component Analyzer). The VNAX is a standard waveguide extension, whereas the VCA has an additional interface for injecting broadband signals towards the DUT. The extenders are connected to port 1 and port 2 of a VNA with spectrum-analyzer option, enabling CW characterization as well as

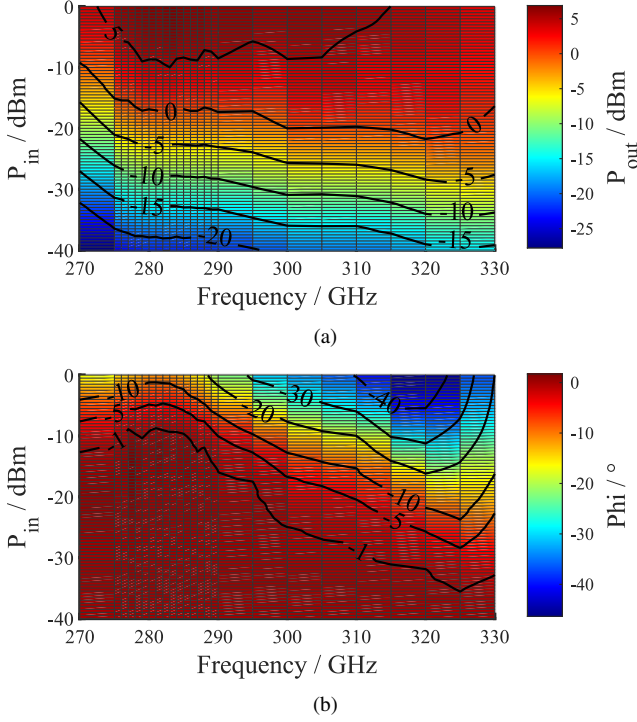


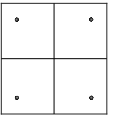
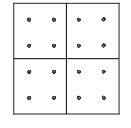
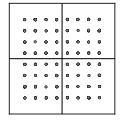
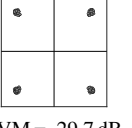
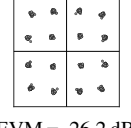
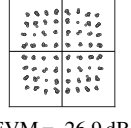
Fig. 3: Measured CW large signal behavior showing (a) gain compression over input power and frequency and (b) phase change of the output tone related to input power and center frequency.

broadband signal acquisition in frequency domain. A wide-band modulated signal, replayed in a continuous loop by an Arbitrary Waveform Generator (AWG) is up-converted to a center frequency within the WR-3.4 waveguide band. Usage of an local oscillator from port 3 of the VNA and a sensitive clock synchronization of the AWG are a premise for phase consistency throughout the setup. A band-pass filter filters unwanted Local Oscillator (LO) leakage or mirror images from the up-conversion. The amplitudes and phases of the wideband signal at port 1 and port 2 are measured. Applying an Inverse Fourier Transform, the time domain representation of the signals can be composed. Using the receiver at port 1, at the input of the DUT, the test signal can be corrected to cancel the impairments of the upconversion stage. With this approach, an isolated view on the DUT with wideband signals is enabled in almost distortion-free conditions.

#### A. Device Under Test: THz Power Amplifier

The DUT used in this work is a 300 GHz WR-3.4 PA module similar to [18], [19]. The PA circuit is realized in a 6-stage topology with cascode and common-source devices, utilizing a 35-nm InGaAs metamorphic high electron mobility transistor (mHEMT) technology. The PA module is implemented in a split-block packaging technology. An E-field-probe-based transition from the Monolithic Microwave Integrated Circuit (MMIC) to the WR-3.4 waveguide, is implemented directly on the GaAs substrate. The PA reaches on average 20 dB gain and 7 dBm of saturated output power within its band of operation from 270 GHz to over 330 GHz.

TABLE I: Measured constellation diagrams from cross-domain characterization at 280 GHz center frequency and 1 GBd symbol rate.

	QPSK	16-QAM	64-QAM
① Corrected Signal at PA input	 EVM = -44.4 dB $P_{in} = -12.9$ dBm	 EVM = -46.2 dB $P_{in} = -13.2$ dBm	 EVM = -43.5 dB $P_{in} = -13.1$ dBm
② Signal at PA output	 EVM = -29.7 dB $P_{out} = +3.3$ dBm	 EVM = -26.2 dB $P_{out} = +3.0$ dBm	 EVM = -26.9 dB $P_{out} = +2.8$ dBm

#### B. Characterization

Fig. 3 shows the vectorial CW-characterization of the PA over both frequency and input power  $P_{in}$ , in terms of AM-AM and AM-PM relations. Sub-figure (a) shows the compression of the output power  $P_{out}$ . A saturated output power of approximately 7 dBm is reached. The curve indicates the varying gain over the frequency and the non-constant spacing between the equi-power lines attests to different compression curves over frequency. Further, in sub-figure (b), the phase modulation is plotted, which is showing major dependency between the phase modulation and the operation frequency. The normalized phase shift  $\Phi$  is defined as the difference of the measured phase shift, compared to the phase shift measured at the linear operation point with  $P_{in} = -40$  dBm at the same frequency, which can be written as

$$\Phi(f, P_{in}) = \phi_{2,1}(f, P_{in}) - \phi_{2,1}(f, P_{in} = -40 \text{ dBm}). \quad (1)$$

This AM-AM and AM-PM data is used in Section IV to extract the behavioral models.

However, to assess the modulation quality and to compare the behavioral models with the actual behavior of the DUT, broadband measurements are carried out. With a baudrate of 1 GHz and modulation formats of QPSK, 16-QAM and 64-QAM, the signal quality in terms of Error Vector Magnitude (EVM) is measured in the cross-link testbench. The EVM is defined as the Root Mean Square (RMS) of the error vector divided by the maximum signal vector of the reference constellation in logarithmic scale. Because of the vectorial calibration capabilities, the influence of the measurement setup, the up- and down-conversion can be corrected from the measurement and solely the influence of the DUT is included. With vector averaging even the noise contribution is reduced to a level, where 45 dB of signal-to-noise ratio is achieved in the measurement. Some exemplary constellation diagrams, where the PA is operated in compression, are shown in the figures in Table I.

#### IV. POWER AMPLIFIER NON-LINEARITY MODELING

In this section, we derive four different AM-AM and AM-PM distortion models based on empirical narrow-band measurement data using polynomial approximation, Rapp, Ghorbani and Saleh models.

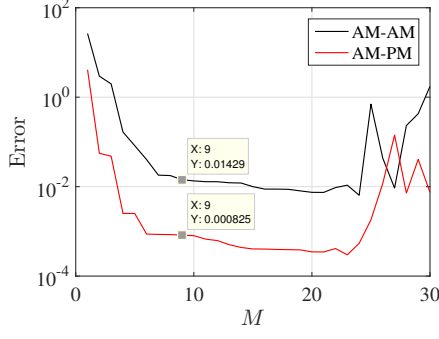


Fig. 4: Fitting error of AM-AM and AM-PM polynomial models.

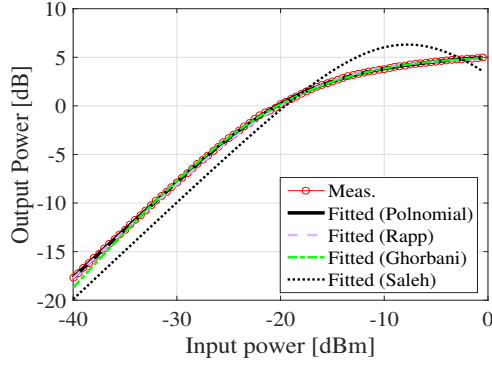


Fig. 5: Polynomial, modified Rapp, Ghorbani and Saleh AM-AM models at 315 GHz.

#### A. Polynomial amplifier model

Similar to [8], a polynomial PA model is derived based on AM-AM and AM-PM data at specific narrow-band operating frequency. The RMS input power range for this model is  $\mathbb{A} \in [-40, 0]$  dBm. The model provides the relationship between output power (RMS) and output phase with respect to input power, measured in dBm, which can be written as

$$\alpha_o = \sum_{m=0}^M a_m \alpha_i^m, \quad \vartheta_o = \sum_{m=0}^M b_m \alpha_i^m. \quad (2)$$

The polynomial coefficients are derived based on a least-squares arrangement using the “polyfit” function defined in MATLAB<sup>®</sup>. Fig. 4 shows the error between the model and the measurement data as a function of the polynomial order  $M$ . The reason for the poor performance of the polynomial fitting, for polynomial orders above 20, is the increased sensitivity to rounding errors. Thus, the choice of lower order polynomials should be made both to reduce the complexity and to avoid the loss of accuracy observed with higher order polynomials. The lowest error is achieved with  $M=24$  (AM-AM) and 23 (AM-PM) however, we consider  $M=9$  as in the model provided in [8] which results in an acceptable performance. Fig. 5 and 6 depict the derived models for  $f_c=315$  GHz and compares them with the measurement. The polynomial coefficients for the polynomial AM-AM and AM-PM behaviors for  $f_c = 315$  GHz are listed in Table II. The coefficients relating to the rest of the frequencies are given in [24].

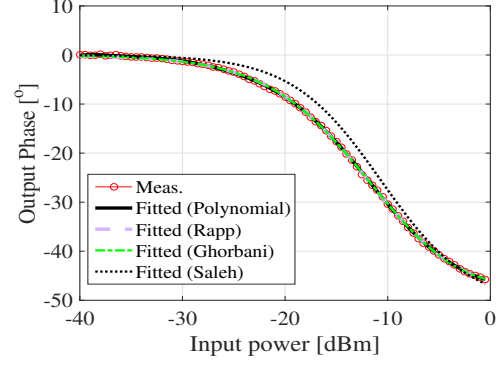


Fig. 6: Polynomial, modified Rapp, Ghorbani and Saleh AM-PM models at 315 GHz.

#### B. Ghorbani model

The Ghorbani PA nonlinearity model [27] characterizes both the AM-AM ( $G_A(x)$ ) and AM-PM ( $G_P(x)$ ) responses using a four parameter equations of the form

$$G_A(x) = \frac{y_1 x^{y_2}}{(1 + y_3 x^{y_2})} + y_4 x, \quad (3)$$

$$G_P(x) = \frac{z_1 x^{z_2}}{(1 + z_3 x^{z_2})} + z_4 x, \quad (4)$$

where the parameter  $y_i, z_i, i \in \{1, 2, 3, 4\}$ , are estimated from the measurements data using curve fitting techniques. The fitting results are depicted in Figs. 5 and 6. To derive the fitting parameters, we adopt the second norm of the difference between the raw measurement data and the Ghorbani model as a cost function, i.e.

$$\varepsilon = \|\mathbf{d}_{\mathcal{M}} - \mathbf{g}_{\mathcal{M}}\|_2, \quad (5)$$

where  $\mathbf{d}$  is the raw measurement data vector,  $\mathbf{g}$  is the Ghorbani model vector,  $\mathcal{M} \in A, P$  with  $A$  and  $P$  representing the AM-AM and AM-PM functions, respectively. Then, we use the MATLAB<sup>®</sup> core function “fminsearch”, which is a nonlinear programming solver, to find the fitting parameters of the model. The Ghorbani AM-AM and AM-PM coefficients for  $f_c=315$  GHz were found to be:  $y_1 = 101.934$ ,  $y_2 = 1.26$ ,  $y_3 = 1728.859$ ,  $y_4 = -0.0174$ , and  $z_1 = -1.667 \times 10^5$ ,  $z_2 = 1.678$ ,  $z_3 = 2.981 \times 10^3$ ,  $z_4 = 1.418 \times 10^2$ . The coefficients for the rest of the operating frequencies are available in [24]. Although the derived parameters properly fit the measurements data as shown in Figs. 5 and 6, we point out that the global optimum cannot be guaranteed since the optimization problem is underdetermined. Other optimization tools can be used to derive the parameters.

#### C. Saleh model

The Saleh PA nonlinearity modeling [28] was specifically derived for traveling-wave-tube amplifiers. The AM-AM and



TABLE II: Coefficients of polynomial amplifier model.

$m$	0	1	2	3	4	5	6	7	8	9
$a_m$	4.93685	-0.0137525	-0.0376565	-0.00671547	-0.000751183	-4.90554e-05	-2.02848e-06	-5.08754e-08	-6.93973e-10	-3.92275e-12
$b_m$	-46.00981	-0.475385	0.172884	0.029412	0.00550807	0.000508238	2.42772e-05	6.33498e-07	8.63223e-09	4.82313e-11

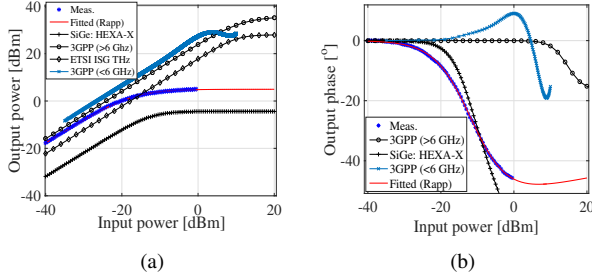


Fig. 7: Comparisons between different AM-AM and AM-PM models.

AM-PM equations can be implemented by respectively applying

$$S_A(x) = \frac{\alpha_1 x}{(1 + \beta_1 x^2)}, \quad (6)$$

$$S_P(x) = \frac{\alpha_2 x^2}{(1 + \beta_2 x^2)}. \quad (7)$$

Given their simple forms, Saleh proposed a general form of  $S_A(x)$  and  $S_P(x)$  given by

$$z(x) = \frac{\alpha x^n}{(1 + \beta x^2)^\nu}, \quad (8)$$

where  $n \in \{1, 2, 3\}$ ,  $\nu \in \{1, 2\}$ . Then, defining  $w_m = \frac{1}{\sqrt{\frac{\nu}{x_m^n}}}$ , the optimal coefficients  $\alpha$  and  $\beta$  in the mean-square-error sense may be written as [28]

$$\alpha = \left[ \frac{(\sum_{m=1}^N x_m^2)^2 - N \sum_{m=1}^N x_m^4}{(\sum_{m=1}^N x_m^2)(\sum_{m=1}^N w_m x_m^2) - (\sum_{m=1}^N x_m^4)(\sum_{m=1}^N w_m)} \right]^\nu \quad (9)$$

$$\beta = \frac{(\sum_{m=1}^N x_m^2)(\sum_{m=1}^N w_m) - N \sum_{m=1}^N w_m x_m^2}{(\sum_{m=1}^N x_m^2)(\sum_{m=1}^N w_m x_m^2) - (\sum_{m=1}^N x_m^4)(\sum_{m=1}^N w_m)}, \quad (10)$$

where  $N$  denotes the size of the input power vector. Based on the above derivations, the values of the Saleh model parameters at  $f_c = 315$  GHz are  $\alpha_1 = 10.127$ ,  $\beta_1 = 5.995 \times 10^3$  with  $n = 1$ ,  $\nu = 1$  and  $\alpha_2 = -595236.026$ ,  $\beta_2 = 11640.052$  with  $n = 2$ ,  $\nu = 1$ . The rest of the derived parameters operating at different center frequencies are provided in [24].

#### D. Modified Rapp amplifier model

The modified Rapp model mimics the performance of PAs that have a linear gain in the small signal region and a saturation for larger input values due to current and voltage clipping. Unlike the original Rapp model introduced in [29], the approach in [30], which is named the modified Rapp model, includes the effect of AM-PM distortion. The output power ( $F_A$ ) and phase ( $F_P$ ) are expressed as

$$F_A(x) = \frac{Gx}{(1 + |\frac{Gx}{V_{\text{sat}}}|^{2p})^{\frac{1}{2p}}}, \quad F_P(x) = \frac{Ax^{q_1}}{1 + |\frac{x}{B}|^{q_2}}, \quad (11)$$

where  $G$  represents the small signal gain,  $p$  denotes the smoothness factor,  $V_{\text{sat}}$  is the saturation voltage coefficient, and the coefficients  $A$ ,  $B$ ,  $q_1$ ,  $q_2$  are AM-PM distortion curve parameters. To derive the modified Rapp parameters, we adopt the same approach as that defined in Section IV.B for the Ghorbani model. The Rapp AM-AM and AM-PM coefficients for  $f_c = 315$  GHz are:  $G = 13.07$ ,  $V_{\text{sat}} = 0.0559$  V,  $p = 0.878$ ,  $A = -1.7204 \times 10^5$ ,  $B = 8.5695 \times 10^{-3}$ ,  $q_1 = 1.6949$ ,  $q_2 = 1.7404$ . The results are depicted in Figs. 5 and 6. Reference [24] provides the coefficients of the Rapp PA nonlinearity model for different center frequencies  $f_c$ .

#### E. Frequency dependence

To capture the PA nonlinearity dependence on frequency, we first depict in Figs. 8 and 9 the AM-AM and AM-PM measurements and polynomial behavioral models for various center frequencies, namely  $f_c \in \{280, 300, 320\}$  GHz. As can be seen, there is a significant difference in the responses, emphasizing on the frequency dependence of the AM-AM and AM-PM behaviors for different center frequencies. Moreover, Fig. 10 depicts  $V_{\text{sat}}$  as a function of the operating frequency. The decreasing overall trend is captured in the figure, implying limitations on the transmission power as the frequency increases. This trend is also captured by the fitted first-order polynomial written as

$$V_{\text{sat}}(f) = -2.5585 \times 10^{-13} f + 0.1345, \quad (12)$$

where  $f$  is the frequency in Hz. We note that the values of  $V_{\text{sat}}$  were extracted from the modified Rapp fitted parameters as a function of the operating frequency. The explainability of the AM-AM Rapp parameters is one of the main features that makes this model popular in standardization activities, while for the rest of the derived models, it is challenging to connect the parameters to the physical characteristics of the derived models, although some of them might yield a more accurate fit to the measurements.

#### F. Comparison with different models

We now compare the derived model with models available in the literature as seen in Fig. 7. The models that are selected to be compared with are:

- 3GPP (< 6 GHz): This is a polynomial-fitted model for both AM-AM and AM-PM, which was proposed in [9] for the purpose of evaluating waveforms operating below 6 GHz.
- 3GPP (> 6 GHz): This model is a modified Rapp-fitted model, which was proposed in [9] to evaluate waveforms operating above 6 GHz, namely 30 and 70 GHz.
- SiGe-HEXA-X: SiGe-based modified Rapp model, which was proposed in [11], [10] for an operating frequency of 290 GHz.

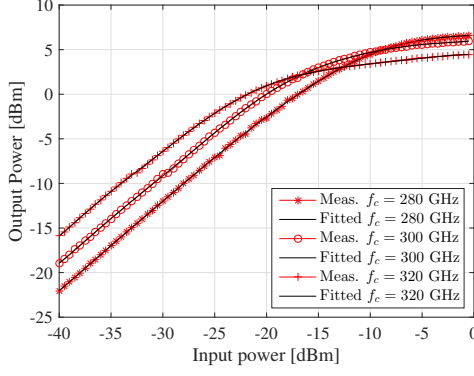


Fig. 8: Different AM-AM measurement data and 9<sup>th</sup> order polynomial behavioral models for different center frequencies.

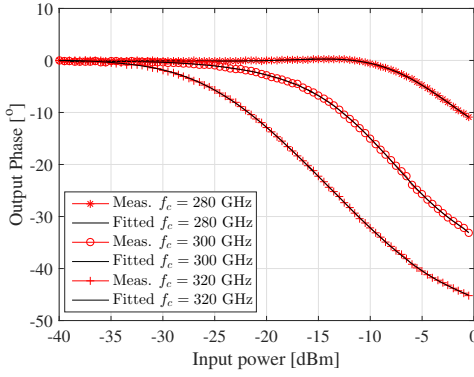


Fig. 9: Different AM-PM measurement data and 9<sup>th</sup> order polynomial behavioral models for different center frequencies.

- ETSI ISG THz-based model, which is a modified Rapp model proposed in [7] for operating frequencies in the 100-200 GHz band, extracted by averaging out the modified Rapp model parameters in the specified frequency range solely targeting AM-AM behavior. Parameters for AM-PM behavior were left unaddressed.

It is worth noting that the 3GPP (< 6 GHz) model is strictly evaluated in the range of input powers  $[-35, 9]$  dBm, which is the range in which the polynomial was fitted, otherwise, the behavior of the model is unreliable. This hints to why the modified Rapp model is preferred over the fitted polynomial model, as the ranges of input power that are fed to the modified Rapp models exceed the range that it was fitted within while still producing an expectable behavioral performance. One notable conclusion of this comparison is the over-estimation of the linear region of the PA models proposed by 3GPP (both higher and lower than 6 GHz), and ETSI ISG THz-based model (which omits the proposal of an AM-PM model) when compared to our derived model. For instance, at an input power value of  $-10$  dBm, the 3GPP (both higher and lower than 6 GHz) and ETSI ISG THz-based models still operate in the linear region for the AM-AM and introduce low phase shift values, while the SiGe-based MMIC and the modeled amplifier produce around  $-30^\circ$  phase shift, and are clearly in the compression region, which is detrimental for even low-

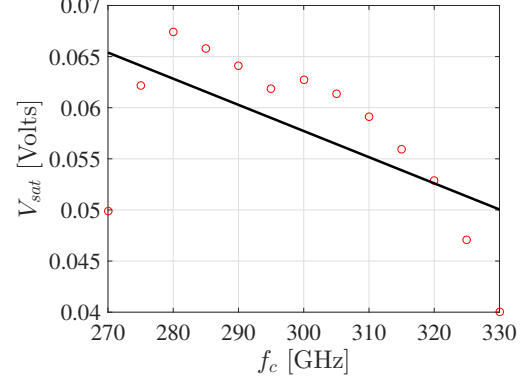


Fig. 10: Rapp-based  $V_{sat}$  vs. operating frequency.

order QAM-based modulation.

### G. Simulation and Comparison to Wideband Measurements

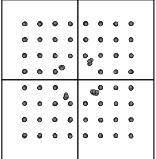
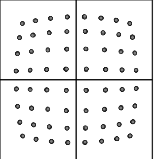
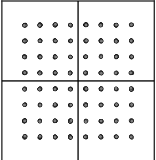
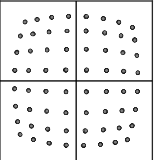
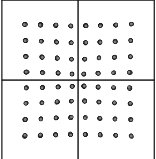
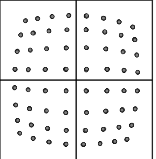
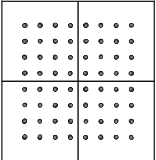
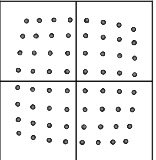
For the assessment of the model accuracy, the models are simulated for single-carrier QAM signals. For each model we consider two center frequencies, 280 GHz and 315 GHz. The results from the 280 GHz simulation are further compared to the wideband measurements from Section III. The simulated constellation diagrams at 280 GHz, each for the lowest and highest input powers can be observed in Table III. The Rapp model and the Saleh-model are showing similarly good results at all power levels. The polynomial model is showing inaccuracies for the lowest input powers. Although the RMS signal power lies within the definition range of the polynomial model, the instantaneous envelope power of the inner constellation points are exceeding the range at which the model has been extracted. Similarly, the Ghorbani model shows inaccurate modeling for lower input powers. Fig. 11 shows a comparison of the EVM for all considered models and compares the simulated gain drop in the upper part of each plot. All models show a similar increase of EVM due to compression, which also aligns with the EVM measurement. However, in linear operation, polynomial and Ghorbani model are inaccurate. This issue is especially pronounced for higher order QAM-modulations like 64-QAM, because of the higher variance in amplitude states. For multi-carrier signals, this effect would be increased due to the even higher spread in amplitude states. For the 280 GHz models, the gain decrease of the band power  $\Delta G$  is captured equally good by all implementations, which is defined by applying

$$\Delta G = P_{out} - P_{in} - S_{21}. \quad (13)$$

With the difference of  $P_{out}$  and  $P_{in}$  being the simulated gain, normalized to the measured small-signal gain  $S_{21}$ . For the 315 GHz models, only the Rapp model is able to reflect the gain compression correctly at all power levels.

We thus conclude that, out of the observed models, only the Rapp model should be considered for accurate system-level modeling. The modified Rapp model follows closely the measured EVM when linear equalization is applied, as shown in Fig. 11 (a) and 11 (b). This leads to the assumption, that

TABLE III: Comparison of the simulated output signals with the implemented PA-models at 280 GHz.

	64-QAM simulated with $P_{in} = -30$ dBm	64-QAM simulated with $P_{in} = -13.2$ dBm
Polynomial model	 EVM = -30.8 dB $P_{out} = -11.4$ dBm	 EVM = -26.9 dB $P_{out} = 3.3$ dBm
Rapp model	 EVM = -42.7 dB $P_{out} = -10.9$ dBm	 EVM = -25.4 dB $P_{out} = 3.8$ dBm
Ghorbani model	 EVM = -34 dB $P_{out} = -11.4$ dBm	 EVM = -25.0 dB $P_{out} = 3.6$ dBm
Saleh model	 EVM = -42.7 dB $P_{out} = -11.6$ dBm	 EVM = -27.2 dB $P_{out} = 3.8$ dBm

PA distortion can be modeled accurately with memory-less PA-models in conjunction with linear memory-effects.

Although the small signal region generally shows an underestimation of the EVM when it is computed using the developed models, a gradual agreement between the simulated and measured values is observed as the input power increases. Increasing the input power yields high output power values that are likely to be adopted *to meet link budget requirements*. In other words, we expect the PA to operate mainly in proximity to the saturation region, where there is a good agreement between the measured distortions and those predicted by our quasi-memoryless models, which can then be used effectively for system performance analysis.

## V. PREDISTORTION ALGORITHM

In this section we describe and analyze the predistortion algorithm used to mitigate the non-linear effects of the PA. We start with the AM-AM and AM-PM characteristics provided by the modified Rapp model (as in (11)) based on the discussions in Section IV, and derive the ideal predistortion function necessary to achieve perfect linearization. Specifically, we determine the inverse AM-AM characteristic and

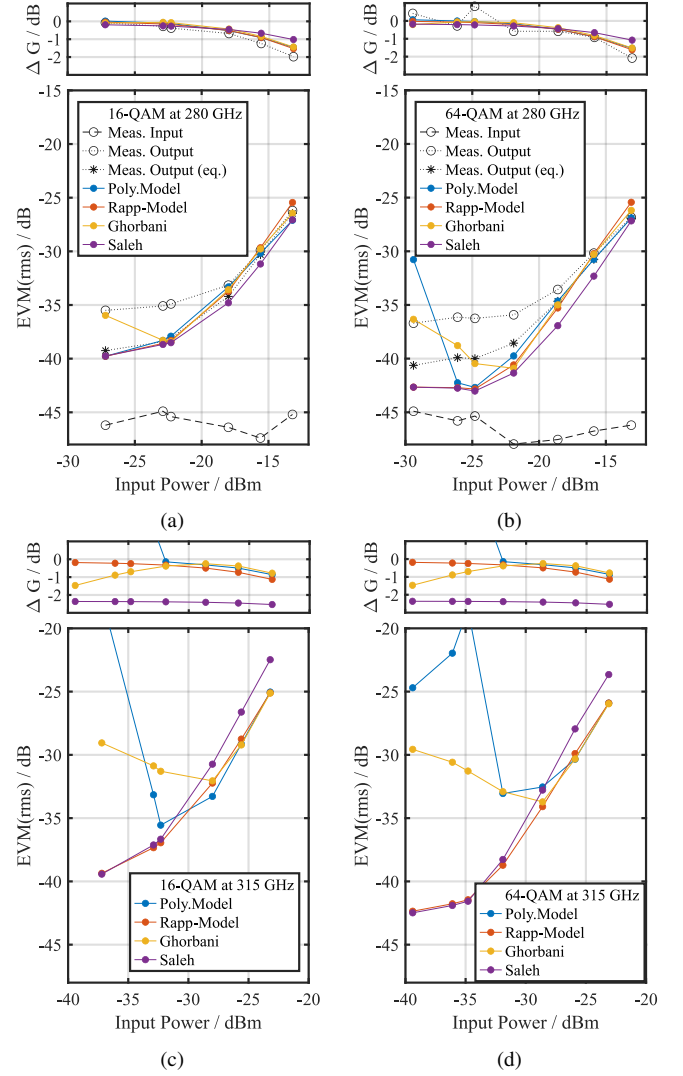


Fig. 11: Comparison of the simulated EVM and gain-drop  $\Delta G$  of the different non-linear models. (a) and (b) are showing 16-QAM and 64-QAM at 280 GHz, supported by measured data. (c) and (d) are showing simulations for models extracted at 315 GHz.

the required AM-PM compensation. Practical implementation of the predistorter is then addressed, focusing on polynomial approximations of the ideal predistortion functions.

The signal  $x(t)$  at the input of the predistorter in Fig. 1 is a two-dimensional signal,  $x(t) = (x_I(t), x_Q(t))$  where  $x_I(t)$  and  $x_Q(t)$  are the In-phase and Quadrature components as usual. For mathematical convenience,  $x(t)$  will be represented as a complex signal  $\tilde{x}(t) = x_I(t) + jx_Q(t)$ . Similarly,  $y(t) = (y_I(t), y_Q(t))$  will be described through  $\tilde{y}(t) = y_I(t) + jy_Q(t)$ . The signal at the output of the RF converter can be written as

$$\begin{aligned} y_{RF}(t) &= y_I(t) \cos(2\pi f_c t) - y_Q(t) \sin(2\pi f_c t), \\ &= \rho_y(t) \cos(2\pi f_c t + \theta_y(t)), \end{aligned} \quad (14)$$

where

$$\rho_y(t) = \sqrt{y_I^2(t) + y_Q^2(t)} \quad \theta_y(t) = \tan^{-1} \left( \frac{y_Q(t)}{y_I(t)} \right). \quad (15)$$



Based on (11), the output of PA is given by

$$z(t) = F_A(\rho_y(t)) \cos(2\pi f_c t + \theta_y(t) + \phi(t)), \quad (16)$$

with  $\phi(t) = F_P(\rho_y(t))$ . From (16), it is clear that the output amplitude and phase distortion,  $F_A(\rho_y(t))$  and  $F_P(\rho_y(t))$ , respectively, depend only on  $\rho_y(t) = |\tilde{y}(t)|$ . This means that the predistortion algorithm can effectively operate on the baseband signals  $\tilde{x}(t)$  and  $\tilde{y}(t)$ .

A key assumption made here is that PA is a memoryless device, meaning that the output is only a function of the instantaneous input. Accordingly, for the sake of simplicity, we drop the dependence on time from all the signals.

#### A. Ideal Predistortion Functions

We start by representing  $z$  with its complex envelope  $\tilde{z}$ , i.e.,

$$\tilde{z} = \rho_z e^{j\theta_z} \quad (17)$$

where

$$\rho_z = F_A(\rho_y) \quad \theta_z = \theta_y + F_P(\rho_y). \quad (18)$$

Ideally, we want the PA output  $z$  to satisfy

$$z = Gx, \quad (19)$$

or, equivalently,

$$\begin{cases} \rho_z = G\rho_x \\ \theta_z = \theta_x, \end{cases} \quad (20)$$

with  $\rho_x = \sqrt{x_I^2 + x_Q^2}$  and  $\theta_x = \tan^{-1}(x_Q/x_I)$ . Let  $A_{PD}(\rho)$  be the amplitude function of the predistorter, i.e.,

$$\rho_y = A_{PD}(\rho_x), \quad (21)$$

where  $\rho_x$  and  $\rho_y$  are the amplitudes at the input and output of Predistortion (PD), respectively. To achieve perfect linearization of the PA, the amplitude input-output response of the predistorter must be the inverse of the PA's response, i.e.,

$$F_A[A_{PD}(\rho_x)] = G\rho_x. \quad (22)$$

Denoting by  $F_A^{-1}$  the inverse of  $F_A(\cdot)$ , we have

$$A_{PD}(\rho_x) = F_A^{-1}[G\rho_x]. \quad (23)$$

The inverse of  $F_A(\cdot)$  can be computed as

$$F_A^{-1}(G\rho_x) = \frac{\rho_x}{\left[1 - \left(\frac{G\rho_x}{V_{sat}}\right)^{2p}\right]^{\frac{1}{2p}}}. \quad (24)$$

As for phase predistortion, based on (18) and (20) we write

$$\theta_y = \theta_x - F_P(\rho_y). \quad (25)$$

Since  $\theta_x$  can easily be obtained by the input signal  $x$ , we just need to compensate for  $F_P(\rho_y)$  for implementing an ideal phase predistortion. Accordingly,  $\theta_y$  is generated as

$$\theta_y = \theta_x + \Theta(\rho_y), \quad (26)$$

where  $\Theta(\rho) = -F_P(\rho)$  is the ideal phase predistortion function. A schematic diagram of PD is reported in Fig. 12. It is worth noting that, due to the discontinuity in the inverse function  $F_A^{-1}(\cdot)$  at  $\rho_x = V_{sat}/G$  (as can be seen from (24)),

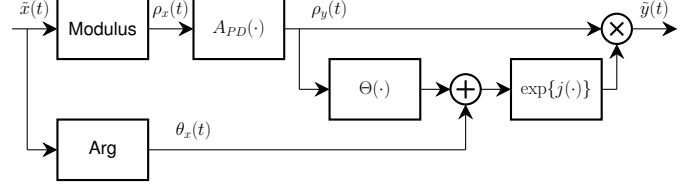


Fig. 12: Schematic diagram of the predistortion device

the signal amplitude at the input of PD must be limited through clipping. We denote by  $\chi$  the clipping level at the input of PD and by  $\gamma$  the corresponding clipping value at the output, i.e.,  $\gamma = A_{PD}(\chi)$ . The impact of  $\chi$  on system performance will be analyzed in detail in Section VI.

#### B. Approximations of the ideal predistortion functions

The ideal amplitude and phase functions of the predistorter, i.e.,  $A_{PD}(\rho_x)$  and  $\Theta(\rho_y)$ , can be approximated by polynomial models [31] defined as

$$A_{PD,\text{poly}}(\rho) = \sum_{k=0}^{N_A} \eta_k \rho^k, \quad \Theta_{\text{poly}}(\rho) = \sum_{k=0}^{N_\theta} \nu_k \rho^k. \quad (27)$$

The coefficients  $\eta_k$  and  $\nu_k$  are obtained through a least-squares (LS) approach, by minimizing the following objective functions:

$$\int_0^\chi \left[ A_{PD}(\rho) - \sum_{k=0}^{N_A} \eta_k \rho^k \right]^2 d\rho, \quad (28)$$

$$\int_0^\gamma \left[ \Theta(\rho) - \sum_{k=0}^{N_\theta} \nu_k \rho^k \right]^2 d\rho. \quad (29)$$

The impact of  $N_A$  and  $N_\theta$  on the system performance will be discussed in the next section.

## VI. SIMULATION RESULTS

Here we analyze the impact of the design parameters  $\chi$ ,  $N_A$  and  $N_\theta$  on system performance, and discuss the possible trade offs between performance and predistortion algorithm complexity. Throughout this section, we will consider the communication system depicted in Fig. 1, and we will assume that the input symbols belong to an  $M$ -QAM constellation, with  $M = 64$ , the modulator uses a square-root raised-cosine filter [25, Chap. 9] with a rolloff factor of 0.5, and the carrier frequency is  $f_c = 315$  GHz.

a) *Clipping*: Fig 13 shows the amplitude of the signals at the PA output with no predistortion algorithm (red curve), at the output of the predistortion block (black curve), and at the output of PA in the presence of an ideal predistorter (blue curve), as a function of the amplitude of the input signal  $x(t)$ . Looking at the black curve (PD output), we can observe that, as the input amplitude approaches the  $V_{sat}/G$  threshold (marked by the purple dashed line), the amplitude of  $y(t)$  increases dramatically, as expected from (24). In order to keep  $|y(t)|$  within reasonable values, the input amplitude  $|x(t)|$  must be clipped at a level below the threshold  $V_{sat}/G$ , while still

providing effective linearization of the PA's response. From Section IV-D, we have  $V_{sat} = 0.0559$  V and  $G = 13.0732$ , so that the threshold is about  $4.28 \times 10^{-3}$  V.

Comparing the blue curve (PA + Ideal PD) to the original PA response (red curve), we can see that the predistortion algorithm provides a nearly linear behavior up to an input amplitude of about  $4 \times 10^{-3}$  V. The improvement is particularly evident in the mid-range region (between  $1.5 \times 10^{-3}$  V and  $3.5 \times 10^{-3}$  V) where the original PA shows a significant compression. Based on the results in Fig 13, we fix the clipping level at  $\chi = 4 \times 10^{-3}$  V.

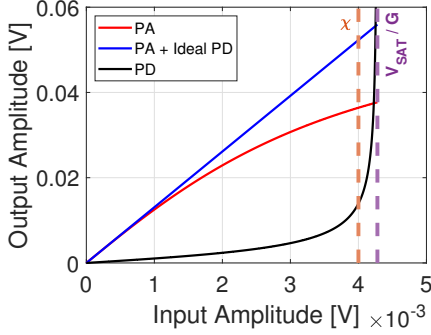


Fig. 13: Output amplitude comparison between PA, PD, PA+PD

*b) Polynomial Order:* The impact of the polynomial approximation order ( $N_A, N_\theta$ ) is analyzed to evaluate performance and complexity trade-off. In doing so, we assume that the modulated waveform  $x(t)$  corresponds to an OFDM signal with  $N_{sc} = 256$  subcarriers. Our analysis is carried out for different values of the Input Back-Off (IBO), which is the difference, measured in decibels (dB), between the average power of  $x(t)$  and the 1-dB compression point of the PA.

Fig. 14a shows the average power at the PA input as a function of IBO, with a fourth-order polynomial approximation, i.e.,  $N_A = N_\theta = 4$ . For comparison, in the same figure we report the results without predistortion and for an ideal predistorter with the same clipping-level  $\chi = 0.004$  V. As can be seen, at low IBO values the predistorted signal exhibits a higher average power compared to the non-predistorted case, meaning that the linearization of the PA requires additional power when we are close to the compression point, as expected. In particular, the curve of the polynomial approximation is close to the curve of the ideal predistorter. As IBO increases, the curve of the polynomial predistorter shows considerable oscillations around the optimal value, meaning that, at high IBO values, a fourth-order polynomial approximation is not a good choice.

Similar behaviors can be observed with an eighth-order polynomial approximation, as shown in Fig. 14b. However, compared to the fourth-order case, we observe that the polynomial approximation and the ideal predistorter are very close, also at high IBO values. Accordingly, we expect to obtain almost ideal performance when using  $N_A = N_\theta = 8$ , at the price of increased complexity.

Although the results in Fig. 14 have been obtained with a multi-carrier signal characterized by  $N_{sc} = 256$ , the same

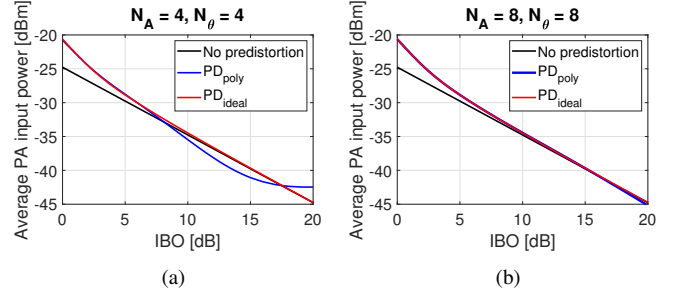


Fig. 14: Average PA input power vs. IBO for different PD polynomial approximation orders.

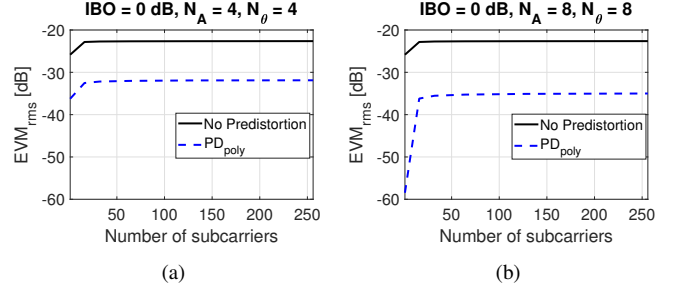


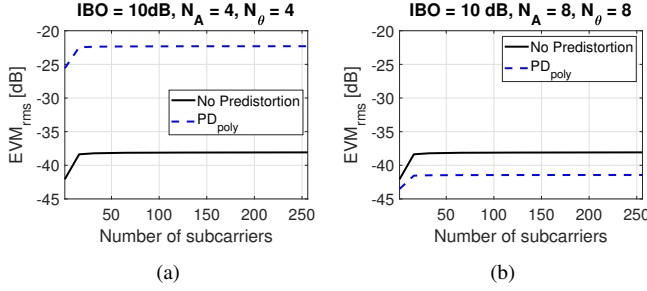
Fig. 15: EVM vs  $N_{sc}$ , IBO = 0 dB

conclusions can be drawn for different values of  $N_{sc}$  and for single-carrier waveforms.

*c) Error Vector Magnitude Analysis:* In this section, system performance in terms of EVM is evaluated for different configurations to assess the impact of the polynomial order. In particular, our analysis focuses on the behavior of EVM as a function of the number of subcarriers, providing important insights into system performance scalability. EVM has been evaluated by simulation, considering both single-carrier ( $N_{sc} = 1$ ) and multi-carrier signals, with  $N_{sc} = \{16, 32, 64, 128, 256\}$ . In all cases, the bandwidth is  $B = 1$  GHz. For the power amplifier, two different values of IBO have been used, namely, 0 and 10 dB.

Fig. 15a shows EVM as a function of the numbers of subcarriers, for IBO = 0 dB and  $N_A = N_\theta = 4$ . As can be seen, the predistortion algorithm improves the EVM values by approximately 10 dB, compared to the case with no predistorter. This gain is the same for single-carrier and multi-carrier signals. It should be noted that the EVM values are almost insensitive to the number of subcarriers, except when we pass from  $N_{sc} = 1$  to  $N_{sc} = 16$ . Similar conclusions can be drawn from the results in Fig. 15b obtained IBO = 0 dB and  $N_A = N_\theta = 8$ . As expected, increasing the polynomial order provides better performance, with a gain of about 15 dB in the multi-carrier case and 20 dB with a single-carrier signal.

Fig. 16a illustrates EVM as a function of  $N_{sc}$ , for IBO = 10 dB and  $N_A = N_\theta = 4$ . In this case, we observe a significant performance degradation compared to the scenario with no predistortion. This behavior is consistent with the results in Fig. 14a which show that, at high IBO values, the performance of the approximate predistorter is far from that of the ideal one. Passing from  $N_A = N_\theta = 4$  to  $N_A = N_\theta = 8$  provides a substantial improvement, with EVM values that are now lower

Fig. 16: EVM vs  $N_{sc}$ , IBO = 10 dB

than the case of no predistortion, as can be seen from Fig. 16b.

d) *Bit Error Rate analysis:* The Bit Error Rate (BER) of the communication system in Fig. 1 has been analyzed considering a point-to-point link in which the transmit and receive antennas are at a distance  $d$ . The channel is AWGN and the received power  $P_r$  is computed as

$$P_r = P_t \frac{G_t G_r}{(4\pi d/\lambda)^2 \cdot L(f_c, d)}, \quad (30)$$

where  $P_t$  is the power of the transmitted signal,  $G_t$  and  $G_r$  are the transmit and receive antennas gains, respectively,  $\lambda = c/f_c$  is the wavelength,  $c$  being the speed of light in vacuum, and  $L(f_c, d)$  is the atmospheric gaseous attenuation evaluated under standard conditions (Atmospheric pressure: 101.300 kPa, Temperature: 290 K, Water vapor density: 7.5 g/m<sup>3</sup>) as in [32].

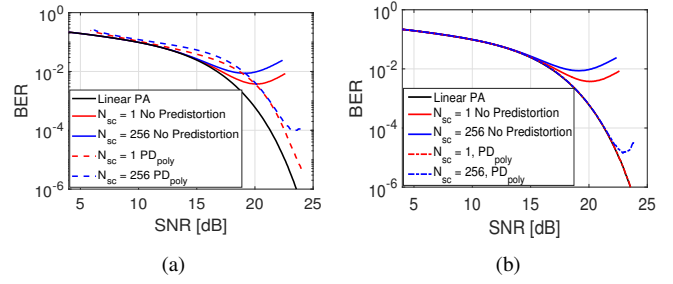
The noise power at the receiver has been computed by using the formula  $\sigma^2 = k_B T_n B$ , where  $k_B$  is the Boltzmann constant and  $T_n$  the equivalent noise temperature. Hence, the signal-to-noise ratio is given by  $\text{SNR} = P_r/\sigma^2$ .

The main system parameters are listed in Table IV.

Parameter	Value
Number of subcarriers	$N_{sc} = \{1, 256\}$
Modulation order	$M = 16, 64$
Transmit antenna gain	$G_t = 45$ dBi
Receive antenna gain	$G_r = 14$ dBi
Bandwidth	$B = 1$ GHz
Noise temperature	$T_n = 290$ K
Center frequency	$f_c = 315$ GHz

TABLE IV: System Parameters

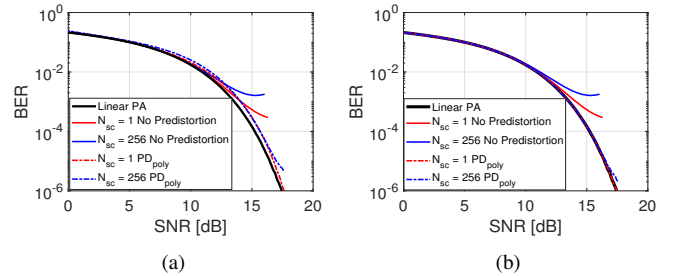
Fig. 17a shows BER as a function of SNR, with  $N_A = N_\theta = 4$ . The modulation order is  $M = 64$ , and the distance between the transmitter and the receiver is  $d = 35$  m. The red curves pertain to the single-carrier case ( $N_{sc} = 1$ ) while the blue curves have been obtained with  $N_{sc} = 256$ . The ideal BER, with a linear PA, and the BER without predistortion have been reported for comparison. It can be seen that, at low SNRs, corresponding to low transmit powers and, hence, to a PA operating in the linear region, the performance without predistortion is virtually identical to that of the ideal system, and is better than that of the system with predistortion. This fact can easily be explained with the results in Fig. 14a which show that, at high IBO values, i.e., in the linear region of the PA, the performance of the polynomial predistorter with  $N_A = N_\theta = 4$  does not coincide with that of the ideal one. As the SNR increases (and IBO decreases) above 16 dB, the BER of the system without predistortion initially decreases (but

Fig. 17: BER vs SNR performance, 64 QAM. (a)  $N_A = 4, N_\theta = 4$ , (b)  $N_A = 8, N_\theta = 8$ 

deviates from the ideal BER) until a minimum is reached, at  $\text{SNR} \approx 20$  dB in the single-carrier case and  $\text{SNR} \approx 18$  dB for  $N_{sc} = 256$ . A further increase in the SNR results in a higher BER due to the uncompensated distortions produced by the PA, which now operates in the non-linear region. Better results can be obtained with the predistortion algorithm. In particular, with  $N_{sc} = 1$ , the predistorted system has a loss of about 1 dB compared to the ideal PA, at least for the SNR values considered in the figure. On the other hand, with the multi-carrier waveform a minimum BER  $\approx 10^{-4}$  can be achieved with an  $\text{SNR} \approx 23.5$  dB. For  $\text{SNR} > 23.5$  dB, the polynomial predistorter is unable to compensate for the PA distortions, and the BER increases.

Similar trends can be observed in Fig. 17b, which illustrates the performance of the polynomial system with  $N_A = N_\theta = 8$ . It is seen that, increasing the polynomial order improves performance significantly, achieving a near-ideal linearization for both single-carrier and multi-carrier waveforms, in a wide range of SNR values.

The same conclusions can be drawn from the results in Fig. 18 which have been obtained with a 16-QAM constellation. In this case, the distance between transmitter and receiver is  $d = 70$  m. As can be seen, the predistortion algorithm achieves good performance with both  $N_A = N_\theta = 4$  and  $N_A = N_\theta = 8$ , and provides substantial improvements compared to the case of no compensation of the PA non-linearities. Also, marginal differences can be observed between the bit error rates in the single-carrier case and in the multi-carrier case.

Fig. 18: BER vs SNR performance, 16 QAM. (a)  $N_A = 4, N_\theta = 4$ , (b)  $N_A = 8, N_\theta = 8$ 

Simulation results – that have not been reported to avoid overloading the figures – indicate that reducing the number of subcarriers (in particular, passing from  $N_{sc} = 256$  to  $N_{sc} =$

16) has a negligible effect on BER performance, as expected from the EVM behavior illustrated in Fig. 15 and Fig. 16.

## VII. DISCUSSION AND CONCLUDING REMARKS

In this paper, the characterization of the behavior of a PA in the 300 GHz band was carried out, where the dependence of the AM-AM and AM-PM behaviors on the operating frequency was captured. Various models have been derived and verified using results from a validation set-up, where a relative accuracy was noted in modeling the errors resulting from distortions in the compression region. The parameters of different AM-AM and AM-PM distortion behavioral models are provided for different operating frequencies, namely Saleh, Ghorbani, polynomial, and the modified Rapp models. Based on the derived models, pre-distortion was applied on single-carrier and multi-carrier (OFDM) waveforms, where performance analysis revealed the impact of several pre-distortion design parameters, such as the order of the polynomial approximation of the inverse AM-AM and AM-PM distortion functions and IBO. The analysis revealed a significant dependence of the error performance when moving from a single-carrier to a multi-carrier set-up, while the error performance did not show any relevant dependency on the number of subcarriers, regardless of the application of pre-distortion. Moreover, the analysis showed that pre-distortion significantly improves the error performance, thus providing the option of reliably adopting multi-carrier waveforms at 300 GHz.

## REFERENCES

- [1] ITU-R, "IMT traffic estimates for the years 2020 to 2030," Tech. Rep. M.2370-0, 2015.
- [2] C. Chaccour, M. N. Soorki, W. Saad, M. Bennis, P. Popovski, and M. Debbah, "Seven Defining Features of Terahertz (THz) Wireless Systems: A Fellowship of Communication and Sensing," *IEEE Communications Surveys and Tutorials*, vol. 24, no. 2, pp. 967–993, 2022.
- [3] *World Radiocommunication Conference 2023 (WRC) - Provisional Final Acts*, 2023.
- [4] "IEEE Standard for Wireless Multimedia Networks," *IEEE Std 802.15.3-2023 (Revision of IEEE Std 802.15.3-2016)*, pp. 1–684, 2024.
- [5] T. Zugno, C. Ciochina, S. Sambhwani, P. Svedman, L. M. Pessoa, B. Chen, P. H. Lehne, M. Boban, and T. Kürner, "Use Cases for Terahertz Communications: An Industrial Perspective," *IEEE Wireless Communications*, vol. 32, no. 1, pp. 90–98, 2025.
- [6] T. Zugno, L. Samara, M. Boban, P. H. Lehne, and T. Kürner, "Terahertz communications for industrial manufacturing: a use case analysis," in *2023 IEEE Conference on Standards for Communications and Networking (CSCN)*, pp. 136–141, 2023.
- [7] ETSI ISG THz, "TeraHertz technology (THz): RF Hardware Modeling," Group Report 004, January 2025. Available on: [https://www.etsi.org/deliver/etsi\\_gr/THz/001\\_099/004/01.01.01\\_60/gr\\_thz004v010101p.pdf](https://www.etsi.org/deliver/etsi_gr/THz/001_099/004/01.01.01_60/gr_thz004v010101p.pdf).
- [8] 3GPP, "Response LS on realistic power amplifier model for NR waveform evaluation," TSG RAN WG1 Meeting 85, R1-166004, May 2016.
- [9] 3GPP, "Realistic power amplifier model for the New Radio evaluation," TSG RAN WG4 Meeting 79, R4-163314, May 2016.
- [10] A. Nimr *et al.*, "Radio models and enabling techniques towards ultra-high data rate links and capacity in 6G," Deliverable D2.3, March 2023.
- [11] S. P. Singh, T. Rahkonen, M. E. Leinonen, and A. Pärssinen, "A 290 GHz Low Noise Amplifier Operating above  $f_{-}\{max\}/2$  in 130 nm SiGe Technology for Sub-THz/THz Receivers," in *2021 IEEE Radio Frequency Integrated Circuits Symposium (RFIC)*, pp. 223–226, IEEE, 2021.
- [12] S. Tarboush, H. Sameddeen, M.-S. Alouini, and T. Y. Al-Naffouri, "Single-versus multicarrier terahertz-band communications: A comparative study," *IEEE Open Journal of the Communications Society*, vol. 3, pp. 1466–1486, 2022.
- [13] D. Lee, A. Davydov, B. Mondal, G. Xiong, G. Morozov, and J. Kim, "From sub-terahertz to terahertz: challenges and design considerations," in *2020 IEEE Wireless Communications and Networking Conference Workshops (WCNCW)*, pp. 1–8, IEEE, 2020.
- [14] D. He, Z. Zhang, H. Lin, Z. Wu, Y. Huang, and Z. Wang, "Performance comparison of single-carrier and multi-carrier waveforms over terahertz wireless channels," *Digital Communications and Networks*, 2024.
- [15] S. Maki, Y. Yuda, T. Kimura, and A. Nishio, "Generation of OFDM waveform with 4.8 GHz bandwidth passing through terahertz and millimeter-wave bands in Beyond 5G system," *IEICE Communications Express*, vol. 12, no. 12, pp. 599–602, 2023.
- [16] Jan Tubbax, Liesbet Van der Perre, Marc Engels, Hugo De Man, Marc Moonen, "OFDM versus Single Carrier: A Realistic Multi-Antenna Comparison," *EURASIP J. Adv. Signal Process*, 2024.
- [17] C. T. Parisi, S. Badran, P. Sen, V. Petrov, and J. M. Jornt, "Modulations for terahertz band communications: Joint analysis of phase noise impact and papr effects," *IEEE Open Journal of the Communications Society*, vol. 5, pp. 412–429, 2023.
- [18] L. John, A. Tessmann, A. Leuther, P. Neiningner, and T. Zwick, "Investigation of Compact Power Amplifier Cells at THz Frequencies using InGaAs mHEMT Technology," in *2019 IEEE MTT-S International Microwave Symposium (IMS)*, pp. 1261–1264, 2019.
- [19] L. John, A. Tessmann, A. Leuther, P. Neiningner, T. Merkle, and T. Zwick, "Broadband 300-GHz Power Amplifier MMICs in InGaAs mHEMT Technology," *IEEE Trans. THz Sci. Technol.*, 2020.
- [20] I. Kalfass, D. Wrana, B. Schoch, J. Hesler, M. Kohler, J.-P. Teyssier, and J. Dunsmore, "Instrumentation for the Time and Frequency Domain Characterization of Terahertz Communication Transceivers and their Building Blocks," in *2023 IEEE/MTT-S International Microwave Symposium - IMS 2023*, pp. 1030–1033, 2023.
- [21] B. Schoch, D. Wrana, A. Tessmann, and I. Kalfass, "Wideband Cross-Domain Characterization of a W-band Amplifier MMIC," in *2023 53rd European Microwave Conference (EuMC)*, pp. 770–773, 2023.
- [22] J. P. Teyssier, N. Messaoudi, J. Dunsmore, and J. Verspecht, "Deterministic detection and vector band stitching for the measurement of 6G wideband test signals," in *2023 53rd European Microwave Conference (EuMC)*, pp. 766–769, 2023.
- [23] S. Haussmann, D. Wrana, L. Samara, T. Zugno, and I. Kalfass, "Towards system-level modeling of broadband sub-thz amplifiers for wireless communication," in *2025 IEEE Topical Conference on RF/Microwave Power Amplifiers for Radio and Wireless Applications (PAWR)*, pp. 5–7, IEEE, 2025.
- [24] L. Samara *et al.*, "Measurements and behavioral model data for a power amplifier operating at 300 GHz," Zenodo, 2025.
- [25] J. G. Proakis and M. Salehi, *Digital Communications 5th Edition*. McGraw Hill, 2007.
- [26] D. Dupleich, A. Ebert, Y. Völker-Schöneberg, D. Sitdikov, M. Boban, L. Samara, G. Del Galdo, and R. Thomä, "Characterization of propagation in an industrial scenario from sub-6 ghz to 300 ghz," in *2023 IEEE Globecom Workshops (GC Wkshps)*, pp. 1475–1480, 2023.
- [27] A. Ghorbani and M. Sheikhan, "The effect of solid state power amplifiers (SSPAs) nonlinearities on MPSK and M-QAM signal transmission," in *1991 Sixth International Conference on Digital Processing of Signals in Communications*, pp. 193–197, IET, 1991.
- [28] A. A. Saleh, "Frequency-independent and frequency-dependent nonlinear models of TWT amplifiers," *IEEE Transactions on communications*, vol. 29, no. 11, pp. 1715–1720, 1981.
- [29] C. Rapp, "Effects of HPA-nonlinearity on a 4-DPSK/OFDM-signal for a digital sound broadcasting signal," *ESA Special Publication*, vol. 332, pp. 179–184, 1991.
- [30] J. Liebetreu, D. Falconer, T. Kolze, and Y. Leiba, "Proposed System Impairment Models," IEEE 802.16 meeting IEEE 802.16.1pp-00/15, March 2000.
- [31] A. D'Andrea, V. Lottici, and R. Reggiannini, "RF power amplifier linearization through amplitude and phase predistortion," *IEEE Transactions on Communications*, vol. 44, no. 11, pp. 1477–1484, 1996.
- [32] International Telecommunication Union, "Attenuation by atmospheric gases," itu-r recommendation p.676-12, International Telecommunication Union, 2019. Available: <https://www.itu.int/rec/R-REC-P.676/en>.